

Measurement of Spatial Correlation Functions Using Image Processing Techniques

James G. Berryman

This paper was published in
Journal of Applied Physics
Volume 57, Number 7
Pages 2374-2384
April 1985

July 1984

This is a preprint of a paper intended for publication in a journal or proceedings.
Since changes may be made before publication, this preprint is made available
with the understanding that it will not be cited or reproduced without the
permission of the author.



DISCLAIMER

This document was prepared as an account of work sponsored by an agency of the United States Government. Neither the United States Government nor the University of California nor any of their employees, makes any warranty, express or implied, or assumes any legal liability or responsibility for the accuracy, completeness, or usefulness of any information, apparatus, product, or process disclosed, or represents that its use would not infringe privately owned rights. Reference herein to any specific commercial products, process, or service by trade name, trademark, manufacturer, or otherwise, does not necessarily constitute or imply its endorsement, recommendation, or favoring by the United States Government or the University of California. The views and opinions of authors expressed herein do not necessarily state or reflect those of the United States Government thereof, and shall not be used for advertising or product endorsement purposes.

MEASUREMENT OF SPATIAL CORRELATION FUNCTIONS
USING IMAGE PROCESSING TECHNIQUES

James G. Berryman
Lawrence Livermore National Laboratory
P. O. Box 808, L-200
Livermore, CA 94550

Abstract

A procedure for using digital image processing techniques to measure the spatial correlation functions of composite heterogeneous materials is presented. Methods for eliminating undesirable biases and warping in digitized photographs are discussed. Fourier transform methods and array processor techniques for calculating the spatial correlation functions are treated. By introducing a minimal set of lattice-commensurate triangles, a method of sorting and storing the values of three-point correlation functions in a compact one-dimensional array is developed. Examples are presented at each stage of the analysis using synthetic photographs of cross sections of a model random material (the penetrable sphere model) for which the analytical form of the spatial correlations functions is known. Although results depend somewhat on magnification and on relative volume fraction, it is found that photographs digitized with 512 x 512 pixels generally have sufficiently good statistics for most practical purposes. To illustrate the use of the correlation functions, bounds on conductivity for the penetrable sphere model are calculated with a general numerical scheme developed for treating the singular three-dimensional integrals which must be evaluated.

1. INTRODUCTION

An elaborate theoretical machinery is available for calculating the properties of heterogeneous materials if certain spatial correlation functions for the materials are known. Formulas have been published for calculating bounds on dielectric constants, magnetic permeabilities, electrical and thermal conductivities, fluid permeabilities, and elastic constants if the two-point and three-point correlation functions are known [1-3].

The n-point spatial correlation function is a measure of the probability of finding n points (in a specified geometrical arrangement) all lying in the region of space occupied by one constituent of a two-phase material. For example, the one-point correlation function is the probability that any point lies in material 1. The two-point correlation function is the probability that two points a specified distance apart are both in material 1. The three-point correlation function is the probability that all three vertices of a specified triangle lie in material 1.

Since two points lie along a line and three points lie in a plane, it is theoretically possible to measure two-point and three-point as well as one-point correlation functions by carefully examining photographs of cross sections of the material to be analyzed. Such measurements have been made by Corson [4] who took photographs of a selected material, magnified the photograph, superimposed a sampling grid on the photograph, and then recorded the relevant values for each grid point. The correlation functions were subsequently computed by relatively straightforward processing of the tabulated data. Corson's procedure is not automated. It requires that an operator examine each grid point of the photograph, decide what numerical value to assign to that

point, and then type that value onto a computer card. This procedure is prohibitively tedious and time consuming. It is therefore desirable to develop an automated method for obtaining this same information by using the now well-established techniques of image processing.

The purpose of this paper is to take the first steps toward automatic digital processing of photographs to obtain spatial correlations functions. First, the spatial correlations functions to be measured are defined. Then, a model random material is introduced for which (1) the analytical form of the spatial correlation functions is known and (2) synthetic photographs of cross sections of the material may be easily generated by computer. The steps in preprocessing of the digitized photographs to eliminate undesirable biases and warping are presented. Techniques for calculating one-point, two-point, and three-point correlation functions are discussed. A method of sorting and storing the values of three-point correlation functions in a compact one-dimensional array is developed. The procedures are illustrated throughout the paper using the synthetic photographs of the model random material. Comparisons are made between the analytical results and the measured values of the spatial correlation functions. It is found that a digitized image with 512 x 512 pixels gives sufficiently good statistics to provide a good reproduction of the expected values of the spatial correlation functions. The computed correlation functions are then used to calculate bounds on the conductivity for a model material.

2. SPATIAL CORRELATION FUNCTIONS

Many discussions of the definition and properties of spatial correlation functions are available in the literature [1-3]. A recent and most thorough treatment has been given by Torquato and Stell [5]. For the present purposes, it will suffice to define the correlation functions and briefly list those properties which are vital to the subsequent analysis. The discussion is limited to two-phase composite media.

Let $p(\vec{r})$ be the value of some property of a random composite material (e.g., electrical or thermal conductivity, dielectric constant, bulk or shear modulus, etc.) which assumes one of two values (p_0 or p_1) depending on whether \vec{r} is located in a grain of material 0 or material 1. Then define the function

$$f(\vec{r}) \equiv \frac{p(\vec{r}) - p_0}{p_1 - p_0}$$

= 0 for \vec{r} in material 0 (1)

= 1 for \vec{r} in material 1.

Complete knowledge of the local property value $p(\vec{r})$ implies complete knowledge of the stochastic variable $f(\vec{r})$. However, our interest in $f(\vec{r})$ is ordinarily limited to just a few of its statistical properties since these properties are often sufficient to provide estimates or bounds on the macroscopic average of the property $p(\vec{r})$ of interest.

The present discussion is limited to the three spatial correlation functions easily measurable using photographs of cross sections of the material:

$$\hat{S}_1 = \langle f(\vec{r}) \rangle = \phi \quad (2)$$

$$\hat{S}_2(\vec{x}) = \langle f(\vec{r})f(\vec{r} + \vec{x}) \rangle \quad (3)$$

$$\hat{S}_3(\vec{x}_1, \vec{x}_2) = \langle f(\vec{r})f(\vec{r} + \vec{x}_1)f(\vec{r} + \vec{x}_2) \rangle \quad (4)$$

where the brackets indicate a volume average over the spatial coordinate \vec{r} . The volume fraction of constituent 1 is given by ϕ . In writing (2)-(4), it has been assumed that the composite medium is statistically homogeneous so that on the average only the differences in the coordinate values are important. If it is assumed further that the random material is also isotropic, then it can be shown that (letting $x = |\vec{x}|$)

$$\hat{S}_2(\vec{x}) = S_2(x) \quad (5)$$

$$\begin{aligned} \hat{S}_3(\vec{x}_1, \vec{x}_2) &= S_3(x_1, x_2, \mu_{12}) \\ &= S_3(x_2, x_1, \mu_{12}) \end{aligned} \quad (6)$$

where

$$\mu_{12} = \cos \theta_{12} = \vec{x}_1 \cdot \vec{x}_2 / |\vec{x}_1| |\vec{x}_2| \quad (7)$$

if $|\vec{x}_1| > 0$ and $|\vec{x}_2| > 0$. The two-point correlation function $S_2(x)$ is the probability that two points a distance x apart are both in material 1. The three-point correlation function $S_3(x_1, x_2, \mu_{12})$ is the probability that all three vertices of the triangle defined by (x_1, x_2, μ_{12}) lie in material 1.

Since $f^2(\vec{r}) = f(\vec{r})$, it follows easily from the definitions (2)-(4) that

$$S_2(0) = \hat{S}_1 = \phi \quad (8)$$

and that

$$\lim_{\epsilon \rightarrow 0} S_3(\epsilon, x, \mu) = S_2(x). \quad (9)$$

If the random mixture possesses no long range order, then

$$\lim_{x \rightarrow \infty} S_2(x) = \phi^2 \quad (10)$$

and

$$\lim_{\substack{x_1 \rightarrow \infty \\ x_2 \text{ fixed}}} S_3(x_1, x_2, \mu_{12}) = \phi S_2(x_2). \quad (11)$$

Combining (10) and (11) shows that

$$\lim_{x_1, x_2 \rightarrow \infty} S_3(x_1, x_2, \mu) = \phi^3 \quad (12)$$

assuming that $\mu \neq 1$, or, if $\mu = 1$, that the difference $x_1 - x_2$ is not fixed. Since $f(\vec{r}) \leq 1$ for all \vec{r} , elementary bounds on the correlation functions may also be derived such as

$$S_3(x_1, x_2, \mu_{12}) \leq \min [S_2(x_1), S_2(x_2), S_2(x_3)] \leq \max [S_2(x_1), S_2(x_2), S_2(x_3)] \leq \phi, \quad (13)$$

where $x_3 = (x_1^2 + x_2^2 - 2x_1 x_2 \mu_{12})^{1/2}$.

3. PENETRABLE SPHERE MODEL

One very simple model of a two-phase composite has been in use for many years [6] and named variously the "randomly imbedded model of spheres" [7] or the model of "overlapping" or "fully penetrable spheres" [8]. This model assumes that particle centers are distributed randomly (positions are uncorrelated) and that each center is surrounded by a sphere of particle material (say material 0) of fixed radius R . If the density of particle centers is great enough and the sphere radius large enough, the spheres defined in this manner will overlap. We will follow Torquato and Stell [8] and call this the penetrable sphere model.

This model has two distinct advantages for our present course of study: (1) Analytical results are known for the three spatial correlation functions of interest. (2) Synthetic photographs of cross sections of such a material are easily generated by computer.

The analytical solutions for the spatial correlation functions of the penetrable sphere model have been given by various authors [6-8]. The general result for the n -point correlation function is

$$S_n(\vec{x}_1, \dots, \vec{x}_{n-1}) = \exp(-\rho V_n) \quad (14)$$

where ρ is the number density of spheres and V_n is the union volume of n spheres with the fixed radius R and centers at the vertices $\vec{x}_1, \dots, \vec{x}_{n-1}$.

The union volume for one sphere is trivially

$$V_1 = \frac{4\pi}{3} R^3. \quad (15)$$

For two spheres, the union volume is [9]

$$V_2(xR)/R^3 = \begin{cases} \frac{4\pi}{3} \left(1 + \frac{3}{4}x - \frac{x^3}{16}\right) & \text{for } x \leq 2 \\ \frac{8\pi}{3} & \text{for } x \geq 2 \end{cases} \quad (16)$$

The union volume of three spheres centered at the vertices of a triangle with sides aR , bR , and cR is [8]

$$\begin{aligned} V_3(aR, bR, cR) &= V_2(aR) + V_2(bR) + V_2(cR) \\ &\quad + V_3^{\wedge}(aR, bR, cR) - 3V_1 \end{aligned} \quad (17)$$

where the intersection volume of three spheres is given by [10]

$$\begin{aligned} V_3^{\wedge}(aR, bR, cR)/R^3 &= \frac{1}{6}abc + \frac{4}{3}\tan^{-1}\left(\frac{Qabc}{a^2 + b^2 + c^2 - 8}\right) \\ &\quad - a\left(1 - \frac{a^2}{12}\right)\tan^{-1}\left(\frac{2Qbc}{b^2 + c^2 - a^2}\right) \\ &\quad - b\left(1 - \frac{b^2}{12}\right)\tan^{-1}\left(\frac{2Qca}{c^2 + a^2 - b^2}\right) \\ &\quad - c\left(1 - \frac{c^2}{12}\right)\tan^{-1}\left(\frac{2Qab}{a^2 + b^2 - c^2}\right) \end{aligned} \quad (18)$$

with $0 \leq \tan^{-1} \leq \pi$. The factor

$$Q = (R^2 - L^2)^{1/2}/L \quad (19)$$

is defined in terms of the circumradius

$$L/R = abc/[(a+b+c)(a+b-c)(b+c-a)(c+a-b)]^{1/2} \quad (20)$$

of the triangle with sides aR, bR, cR .

To generate a synthetic photograph of a cross section of a block of penetrable sphere material, consider a unit cube (in Cartesian space x, y, z), and suppose the desired cross section has z -coordinate $z = z_0$ where $R \leq z_0 \leq 1-R$. Using a random number generator, we select z -coordinates for particle centers. If the i -th z -coordinate z_i satisfies $|z_0 - z_i| < R$, then the cross section at $z = z_0$ intersects that sphere and our graphics package draws a shaded circle in the x, y -plane centered at x_i, y_i (chosen by random number generator) with radius r_i given by $r_i^2 = R^2 - (z_0 - z_i)^2$. If z_i satisfies $|z_0 - z_i| \geq R$, we continue generating z -coordinates until the acceptance criterion is again satisfied. The total number of z_i 's generated is determined by the desired volume fraction ϕ and the effective magnification of the desired photograph (i.e., a few large particles or many small particles). Two of the three quantities ϕ , R , and ρ may be chosen independently since (14) and (15) show that

$$\phi = \exp(-\rho \frac{4\pi}{3} R^3). \quad (21)$$

In our synthetic examples, we have typically chosen ρ equal to 1000 or 8000 which leads to approximately 100 or 400 circles per cross section. Then, choosing a target volume fraction ϕ determines the sphere radius R . An example of a synthetic photograph generated using this algorithm is illustrated in Figure 1.

This algorithm can also be used to generate synthetic digital data directly. It has been found useful to have both alternatives available. The algorithms for measuring the spatial correlation functions can be tested very well on the synthetic digital data. However, the process of producing a synthetic photograph and then digitizing the photograph allows us to study the inevitable flaws introduced by the particular digitizing process used.

4. PREPROCESSING OF DIGITIZED IMAGES

Flaws in the digitized image of a surface are inevitable. The original photograph may have distortion, blemishes, non-uniformities, grain noise, etc. Furthermore, even if the photograph is "perfect", the process of digitizing the photograph may introduce errors such as (1) geometric warping (e.g., a lens aberration or the photograph not lying perfectly flat while being digitized), (2) loss of resolution (blurring) due to the finite extent of each picture element (pixel), or (3) quantization noise due to the finite number of intensity levels available per pixel. Nonlinearities in the algorithm for converting intensity level to pixel value also complicate the analysis. For the present application, we have chosen to limit discussion to digitized images which are purely black (0) and white (1) to conform to the discussion of Section 2 even though the picture elements are themselves spatial averages of $f(\vec{r})$ in Eq. (1). (This approximation is expected to be satisfactory if the magnification of the cross section is chosen so that the number of pixels occurring at the interfaces is small compared to the total.) To obtain the desired binary digital image requires preprocessing of the record.

Geometric corrections

To detect warp and to aid in its removal, it is helpful to place (for example) a square frame around the surface to be photographed. On the synthetic photographs, such a frame can be added easily using standard graphics software (see Figure 1). For photographs of real surfaces, a frame should be constructed and care should be taken to include the frame in the field of vision during the photography. The frame serves as a reference. If the frame

is not square in the digitized image, steps may be taken to correct the warp. The method used here is to choose several control points along and at the corners of the frame (but just inside) and then to expand and square the picture (now without the frame) so that the desired image occupies the full 512 x 512 pixel area. The expansion is performed using a straightforward bilinear interpolation algorithm (supplied by M. R. Portnoff).

This step in the preprocessing appears to be unavoidable. The frame is necessary to check for warping. However, with the frame in place, the expansion step is required whether or not warping occurs because the frame must not be present in the image used to obtain the spatial correlation functions.

Distribution of pixel values

A digitized "black and white" image typically contains 256 shades of pseudo-gray with values ranging from 0 (black) to 255 (white). If an original black and white photograph (such as Figure 1) has no flaws, then the corresponding digitized image will have most of its pixel values clustered around two values. There will be some spreading of pixel values even in the best of cases because some of the picture elements occur at interfaces between black and white (see Figures 2 and 3). These pixels must have some intermediate value depending on the proportion of black and white contained in its area and on the particular algorithm used for digitization. The distribution of pixel values is illustrated most easily by constructing a histogram of these values for the image (e.g., see Figure 4). This histogram is bimodal and provides most of the information needed to choose the threshold value required for generating the final digitized image containing all zeroes and ones. Since

the two modes in the histogram are widely separated in this example, considerable freedom in the choice of threshold value is still available. Once a threshold value has been chosen, it is straightforward to generate the desired binary image (see Figures 5 and 6). Then a visual comparison of the original digitized image with the binary image is generally sufficient to determine whether the binary image is a satisfactory representation of the original; if not, new threshold values may be chosen and new binary images generated until a satisfactory binary representation is obtained.

Other corrections

Various other flaws such as blemishes and non-uniform photographic fog can occur [see Figure 2(a)]. Most of these flaws can be treated using standard image processing techniques such as clipping and filtering. More detailed treatment of these problems will not be required here, since we assume the reader has some familiarity with digital signal processing techniques.

5. CALCULATING CORRELATION FUNCTIONS

Once any image warping has been removed and the color spread has been treated after choosing an appropriate threshold value, the resulting image file contains only zeroes and ones for the pixel values f_{ij} where $i, j = 1, \dots, 512$. Let $N = 512 \times 512$. Then the estimate of the one-point correlation function from one image is given by

$$\phi = \frac{1}{N} \sum_{ij} f_{ij}. \quad (22)$$

The standard deviation of ϕ is given by

$$\Delta\phi = [\frac{1}{N} \sum_{ij} (f_{ij} - \phi)^2]^{1/2} = \phi^{1/2}(1-\phi)^{1/2} \quad (23)$$

since $f_{ij}^2 = f_{ij}$. Note that (23) is always greater than ϕ if $\phi \leq 0.5$. A more interesting statistical quantity is the variance of measured ϕ 's for images of several cross sections of the same material or for different segments of the same image. We will not explore such statistical questions in detail in the present paper.

Two-point correlations

A two-point correlation function is just an autocorrelation function of the digital image. Although we have assumed statistical homogeneity and isotropy in Eqs. (3) and (5), these assumptions will only be satisfied approximately by any particular image. One discretized version of (3) is

$$\hat{S}_2(m, n) = \frac{1}{N_2} \sum_{\substack{1 \leq i \leq i_{\max} \\ 1 \leq j \leq j_{\max}}} f_{ij} f_{i+m, j+n} \quad (24)$$

where $i_{\max} = 512-m$, $j_{\max} = 512-n$, and $N_2 = i_{\max} \times j_{\max}$, for $0 \leq m, n \leq 511$. Another possibility involves recognizing that (24) is a convolution and, as such, can be performed rapidly using Fourier transform methods. These techniques are well known and are generally available as standard software on most image processing systems so we will not elaborate here.

Given the two-dimensional estimate $\hat{S}_2(m,n)$, we can obtain the desired one-dimensional (isotropic) correlation function $S_2(k)$ by averaging over the \hat{S}_2 values at a fixed radius k . Except for the cases $(0,k)$ and $(k,0)$, $\hat{S}_2(m,n)$ will not generally be known at the points of interest (see Figure 7). Therefore, we define the function

$$S_2(k,\theta) = \hat{S}_2(k \cos \theta, k \sin \theta). \quad (25)$$

Whenever $k \cos \theta$ and $k \sin \theta$ are not both integers, the value of the right hand side of (25) is defined as the bilinear interpolation from the lattice values $\hat{S}_2(m,n)$. Then our choice for the isotropic average of the two-point correlation function is given by

$$S_2(k) = \frac{1}{2k+1} \sum_{z=0}^{2k} S_2(k, \frac{\pi z}{4k}), \quad \text{for } 0 \leq k \leq 256. \quad (26)$$

If the lattice values $\hat{S}_2(m,n)$ were calculated using Fourier convolution, $k = 256$ is the maximum radius which can be calculated this way because of the redundancy of the resulting autocorrelation. If the $\hat{S}_2(m,n)$ were calculated using (24), it is still wise to limit k to 256 or less because of statistical considerations.

For k greater than zero, the individual terms of the sum in (26) may be treated as independent estimates of $S_2(k)$. Thus, an estimate of the standard deviation of $S_2(k)$ is given by

$$\Delta S_2(k) = \left[\frac{1}{2k+1} \sum_{\ell=0}^{2k} S_2^2(k, \frac{\pi\ell}{4k}) - S_2^2(k) \right]^{1/2}, \text{ for } k \geq 1. \quad (27)$$

Figure 8 shows an example of the calculated values of $S_2(k)$ for a synthetic photograph (Figure 2) with $\phi = 0.31$. The illustration includes the expected S_2 calculated using (14) and (16) [the dashed line], the averaged S_2 obtained using (26) [the solid line] and for comparison the two edge estimates $\hat{S}_2(k,0)$ and $\hat{S}_2(0,k)$ [the dot-dash and long-dash/short-dash lines]. As we might expect, all of the estimates agree very well for small k . The averaged S_2 agrees best with the analytical result for all values of k . The edge estimates differ significantly from each other and from the analytical result for larger values of k but tend to oscillate around the predicted values. The statistics appear to be quite good for $k \leq 100$ since the averaged S_2 value stays very close to the analytical result in this region.

Three-point correlations

One discretized version of the definition (4) of a three-point correlation function which can be calculated in a plane is

$$\hat{S}_3(m,n; q,r) = \frac{1}{N_3} \sum_{\substack{1 \leq i \leq i_{\max} \\ 1 \leq j \leq j_{\max}}} f_{ij} f_{i+m,j+n} f_{i+q,j+r} \quad (28)$$

where $i_{\max} = 512-\max(m,q)$, $j_{\max} = 512-\max(n,r)$, and $N_3 = i_{\max} \times j_{\max}$, for $0 \leq m,n,q,r \leq 511$. Although (27) can be computed quite easily, it is very time consuming and the storage requirements for the results are prohibitive. For example, if we limit the arguments to the range $0 \leq m,n,q,r < 64$, the total storage requirement for the four-dimensional array is over 16×10^6 words. If we note that in the isotropic case the value of S_3 depends only on the size and shape of a triangle, it is possible to reduce the storage to a three-dimensional array with about 26×10^4 elements. This amount of storage is within reasonable limits but we can actually do much better than this by using the various symmetries of S_3 .

The most important property of the isotropic S_3 for these purposes is the fact that its value depends only on the size and shape of the triangle specified by its arguments. Thus, if the triangle has sides a,b,c and the cosines of the angles opposite these sides are respectively

μ_a, μ_b, μ_c , then

$$S_3(a,b,\mu_c) = S_3(b,c,\mu_a) = S_3(c,a,\mu_b) \quad (29)$$

while the law of cosines gives

$$\mu_c = \frac{a^2 + b^2 - c^2}{2ab} \quad (30)$$

and permutations. It is important to account for the symmetries (6) and (29) when choosing the scheme for calculating and storing the values of S_3 , otherwise the stored values will be at least six-fold redundant. Furthermore, although it is clearly advantageous to compute only values of S_3 whose triangle

vertices lie exactly on three lattice points, it is not advantageous to compute S_3 for every triangle commensurate with the lattice. A scheme which chooses a minimal set of lattice-commensurate triangles from which any desired values of S_3 can be found by interpolation is believed to be the preferred solution to the sorting and storing problem.

A minimal set of lattice-commensurate triangles can be uniquely determined by the following algorithm: Each triangle will be labelled by three integers (ℓ, m, n) . The first integer (ℓ) is the length of the longest side of the triangle. The vertex of this triangle formed by the intersection of the longest side and the shortest side is then treated as the origin $(0,0)$ of an x, y -coordinate system and the longest side of the triangle is placed along the x -axis so that the second vertex is located at $(\ell, 0)$. The third vertex of the triangle is then located in the first quadrant at (m, n) .

All triangles may be sorted in this manner. The third vertex specified by (m, n) will always lie in a sector of a circle of radius ℓ centered at $(\ell, 0)$, bounded below by the x -axis, and on the right by the line $x = \ell/2$ (see Figure 9). The arc occurs because the side of intermediate length can be equal to but never longer than ℓ . The line at $x = \ell/2$ occurs because the smallest side can be equal to but never longer than the intermediate side. Note that, although all right triangles whose sides adjacent to the right angle are integers are lattice-commensurate triangles, these right triangles are not included in our minimal subset because the corresponding values of S_3 may be computed by interpolation from those values which are included. This point is illustrated in Figure 9 for a right triangle with sides 3, 5, and 5.83 units.

Figure 10 shows the sequence of diagrams used to determine the minimal set of lattice-commensurate triangles for ℓ up to $\ell = 9$. Table 1 lists the number of triangles for each value of ℓ and the total storage requirement T_ℓ for ℓ up to $\ell = 33$. For $\ell = 63$, the number of triangles is 1233 and the total storage requirement is still only $T_{63} = 27095$. The required storage has therefore been reduced by almost an order of magnitude at $\ell = 63$.

The penalty to be paid for reducing the storage requirement is the increased complexity of assigning and later recomputing the one-dimensional address $I_{\ell mn}$ of the elements of the three-point correlation function. The number of triangles and the storage requirement (T_ℓ) as a function of ℓ observed in Table 1 are not easily deduced analytically. In fact, this problem is closely related to a very difficult unsolved problem due to Gauss concerning the number of lattice points in a circle with center at the origin and radius ℓ [11,12]. Lacking an analytical solution to the address problem, a computationally convenient solution is sought.

First, note that, for our minimal set of triangles, the admissible sets of triples (ℓ, m, n) with $0 \leq \ell, m, n$ satisfy

$$m \leq \ell/2 \quad (31)$$

and

$$(\ell-m)^2 + n^2 \leq \ell^2 \quad \text{or} \quad m^2 + n^2 \leq 2m\ell. \quad (32)$$

Next, we choose to assign the addresses $I_{\ell mn}$ so that (1) all addresses with fixed ℓ are contiguous, (2) for given ℓ all addresses with fixed m

are contiguous, and (3) $I_{\ell mn}$ increases whenever ℓ , m , or n increase.

This choice of assignment leads to the following conclusions:

For $\ell = 0, 1$,

$$I_{\ell mn} = 1 + \ell. \quad (33)$$

For $\ell \geq 2$ and $m = 0, 1$,

$$I_{\ell mn} = L_\ell + m(n + 1) \quad (34)$$

where

$$L_\ell = I_{\ell 00} = T_{\ell-1} + 1. \quad (35)$$

Recall that T_ℓ is the storage requirement for all members of the minimal set of commensurate triangles with longest side less than or equal to ℓ (see Table 1). Finally, for $\ell \geq 4$ and $m \geq 2$,

$$I_{\ell mn} = L_\ell + \sum_{p=1}^{m-1} M_{\ell p} + n + 1 \quad (36)$$

where $M_{\ell p}$ is a matrix whose elements are computed once and stored. An element $M_{\ell p}$ is the total number of lattice points with $m = p$ for case ℓ . The matrix elements may be generated very easily using the inequalities (31) and (32). Table 2 illustrates this matrix for $2 \leq \ell \leq 32$.

As examples of the algorithm, we see by using Tables 1 and 2 that $I_{521} = 18 + 4 + 1 + 1 = 24$, that $I_{310} = 6 + 1 = 7$, and that $I_{942} = 85 + 5 + 6 + 7 + 2 + 1 = 106$. The inverse problem for location 55 is solved as follows: First, $T_6 < 55 \leq T_7$, implies $\ell = 7$. Then $55 - T_6 = 12$ is greater than $1 + 4 + 5 = 10$ so $m = 3$. Finally, $n = 55 - (T_6 + 1) - 10 = 1$. Thus, $55 = I_{731}$.

Having established a procedure for sorting triangles and for storing and subsequently retrieving the corresponding values of the three-point correlation function with a compact one-dimensional array, the discussion will now turn to methods of computing the elements of S_3 . The chosen storage algorithm makes the use of Fourier transform methods less desirable for computing S_3 than S_2 . We should tailor our computational algorithm so that only those elements of S_3 which will be stored are computed. In the following discussion, the emphasis will be placed on obtaining an algorithm convenient for use with an array processor. However, the resulting algorithm can also be used conveniently even if an array processor is not available.

The symmetries of S_3 presented in (6) and (29) suggest that the algorithm for computing should contain every possible orientation of the appropriate lattice-commensurate triangle with one vertex at point (i,j) summed over all possible points. Figure 11 shows three possible stencils which could be used with the given triangle. Note that, although Figure 11(a) and 11(b) are independent measures of S_3 for the same central site, they supply redundant information when summed over all sites. Of these two stencils, Figure 11(a) is preferred because the value of every vertex is used at least twice. This feature can be used to advantage in an array processor with a vector-add-add-multiple function. Nevertheless, both Figures 11(a) and 11(b) have one significant disadvantage over Figure 11(c). As the ℓ -value of the commensurate triangle grows, the region of allowed central points shrinks rapidly like $(512-2\ell)^2$. Furthermore, array processors generally cannot hold all 512×512 values of the image file simultaneously. Typically about 102 rows of the image may be stored so the allowed region actually shrinks like $(512-2\ell) \times (102-2\ell)$. This limitation places a severe constraint

on the range of triangles for which S_3 can be computed (i.e., $\ell \leq 50$ is required and realistically $\ell \leq 25$ to obtain good statistics). One alternative is to try a stencil such as Figure 11(c) which uses one triangle from each of Figures 11(a) and 11(b). This stencil has its long axis aligned with the long direction of the stored image and the allowed region shrinks only like $(512-\ell) \times (102-n)$. The use of this stencil places no serious restrictions on the choice of (ℓ, m, n) since other considerations (computing time and storage) for a 512×512 image limit the large side of the triangle to about $\ell \leq 64$.

Figure 12 illustrates the results obtained by using the stencil in Figure 11(c) to calculate S_3 for Figure 2. The curve displayed is only one of the large variety of possible one-dimensional plots of this three-dimensional quantity. The independent variable p is the multiplier in the formula

$$(\ell, m, n) = px(L, M, N) \quad (37)$$

where (L, M, N) determines the shape of a lattice-commensurate triangle and p determines its size. Thus, as p varies from 0 to p_0 , the argument of S_3 varies from $(0, 0, 0)$ to $(p_0 L, p_0 M, p_0 N)$. Figure 12(a) shows the result for S_3 when only 204 lines of the image are used in the computation while Figure 12(b) shows the result using 510 lines. Other examples have been considered using each of the possible multiples of 102 lines and it has been found in general that the computed curves approach the analytical predictions more closely for larger values of p as the number of image lines used increases. Furthermore, it has been found that the agreement using 510 lines is very good (± 0.005) for $\ell \leq 32$ and reasonably good (± 0.02) for $32 \leq \ell \leq 64$. We conclude that, for the synthetic images studied here at the magnifications illustrated in Figures 1, 2, and 4, the use of a single photograph is sufficient

to determine ϕ , S_2 , and S_3 to the desired accuracy for most practical problems. For smaller porosities than those illustrated here, the number of terms contributing to the sums can be comparatively small with a resulting degradation in performance. This statistical problem can be solved by analyzing photographs of several cross sections of the same material in these cases.

The use of these results and some further refinements will be discussed in the next section.

6. BOUNDS ON CONDUCTIVITY

As was mentioned in the Introduction, various formulas providing estimates of physical constants for composite materials are known [3]. Milton [13,14] has recently shown how to simplify some of these formulas by introducing two parameters (ζ_1 and n_1) which depend on the microgeometry of the random composite through the three-point correlation function S_3 . Milton applied this idea to the effective dielectric constant and to the effective bulk and shear moduli of two-phase composites. The corresponding formulas for the electrical and thermal conductivities, the magnetic permeability, and the diffusivity are the same as the ones for the dielectric constant. We will pose the discussion here in terms of the electrical (or thermal) conductivity σ . The more difficult cases of bounds on fluid permeability and bounds on elastic constants for the penetrable sphere model have been treated elsewhere [15,16].

Let the conductivities of the two constituents be σ_0 and σ_1 with the volume fractions ϕ_0 and ϕ_1 respectively ($\phi_0 + \phi_1 = 1$). First, we introduce the function [17]

$$\Sigma(x) = \left\langle \frac{1}{\sigma(\vec{r}) + 2x} \right\rangle^{-1} - 2x . \quad (38)$$

Then it is not difficult to show that Milton's simplified upper (σ^+) and lower (σ^-) bounds [13] are given by

$$\sigma^+ = \Sigma(\langle \sigma \rangle_\zeta) \quad (39)$$

$$\sigma^- = \Sigma(\left\langle \frac{1}{\sigma} \right\rangle_\zeta^{-1}) , \quad (40)$$

where

$$\langle \sigma \rangle_{\zeta} = \sigma_0 \zeta_0 + \sigma_1 \zeta_1 \quad (41)$$

$$\left\langle \frac{1}{\sigma} \right\rangle_{\zeta} = \frac{\zeta_0}{\sigma_0} + \frac{\zeta_1}{\sigma_1} \quad (42)$$

and the zeta Milton numbers are given by $\zeta_0 = 1 - \zeta_1$ and

$$\zeta_1 = \lim_{\Delta \rightarrow 0} \lim_{\Delta' \rightarrow \infty} \frac{g}{2\phi_0^2 \phi_1^2} \int_{-\Delta}^{\Delta'} dr \int_{-\Delta}^{\Delta'} ds \int_{-1}^{+1} d\mu \frac{S_3(r, s, \mu)}{rs} P_2(\mu). \quad (43)$$

In (43), $P_2(\mu)$ is the Legendre polynomial of order 2. The eta Milton number (η_1) is similar in form to (43) but it depends on $P_4(\mu)$ as well as $P_2(\mu)$. The bounds on conductivity do not depend on the η 's so we will not discuss them further here except to note that the analysis which follows applies equally well to them.

To evaluate (43) it is very helpful to use the various limiting behaviors of S_2 and S_3 summarized in Eqs. (8)-(12). Eq. (11) plus the orthogonality properties of the Legendre polynomials are sufficient to guarantee in all cases of practical interest that the upper limit Δ' may be replaced by a finite maximum or cutoff value Δ_c . Similarly, the limit in Eq. (9) and the same orthogonality properties are sufficient to show that singularities of the integrand at the origin are integrable and lead to a finite value for (43). If we introduce a small length Δ_0 and separate the integral in (43) into four contributions to be evaluated independently, then

$$\begin{aligned}
 \frac{5}{2} I(a_2) &= \int_{\Delta_0}^{\Delta_C} dr \int_{\Delta_0}^{\Delta_C} ds \frac{a_2(r,s)}{rs} \\
 &\quad + 2 \int_{\Delta_0}^{\Delta_C} ds \frac{a_2(\Delta_0, s)}{s} \\
 &\quad + a_2(\Delta_0, \Delta_0) + O(\Delta_0^2).
 \end{aligned} \tag{44}$$

The function $a_2(r,s)$ in (44) is the coefficient of $P_2(\mu)$ in the Legendre polynomial expansion of S_3

$$S_3(r,s,\mu) = \sum_{n=0}^{\infty} a_n(r,s) P_n(\mu) \tag{45}$$

given by

$$a_n(r,s) = \frac{2n+1}{2} \int_{-1}^{+1} d\mu S_3(r,s,\mu) P_n(\mu). \tag{46}$$

Note that, for $n \geq 1$, $a_n = 0$ if either $r = 0$ or $s = 0$ and that $a_0(0,s) = S_2(s)$.

The second term in (44) arises by substituting a discretized Taylor expansion for a_2

$$\begin{aligned}
 a_2(r,s) &= a_2(0,s) + \left. \frac{\partial a_2(r,s)}{\partial r} \right|_{r=0} r + \dots \\
 &\approx a_2(0,s) + \frac{a_2(\Delta_0, s) - a_2(0,s)}{\Delta_0} r + \dots \tag{47} \\
 &= a_2(\Delta_0, s) \frac{r}{\Delta_0} + O(r^2)
 \end{aligned}$$

into the subintegrals

$$\begin{aligned} \int_0^{\Delta_0} dr \int_{\Delta_0}^{\Delta_C} ds \frac{a_2(r,s)}{rs} &= \int_U ds \int_{\Delta_0}^{\Delta_C} dr \frac{a_2(r,s)}{rs} \\ &= \int_{\Delta_0}^{\Delta_C} ds \frac{a_2(\Delta_0, s)}{s}. \end{aligned} \quad (48)$$

The third term in (44) is found similarly by writing the discretized version of the double Taylor expansion

$$\begin{aligned} a_2(r,s) &= a_2(0,0) + \left. \frac{\partial a_2(r,s)}{\partial r} \right|_{r=0} \Bigg|_{s=0} r + \left. \frac{\partial a_2(r,s)}{\partial s} \right|_{r=0} \Bigg|_{s=0} s \\ &\quad + \left. \frac{\partial^2 a_2(r,s)}{\partial r \partial s} \right|_{r=0} \Bigg|_{s=0} rs + \dots \\ &\sim \frac{a_2(\Delta_0, \Delta_0) - 2a_2(\Delta_0, 0) + a_2(0, 0)}{\Delta_0^2} rs + \dots \\ &= a_2(\Delta_0, \Delta_0) \frac{rs}{\Delta_0^2} + \dots . \end{aligned} \quad (49)$$

The usefulness of (44) depends on the smallness of the neglected terms of $O(\Delta_0^2)$ which depend on second and higher derivatives of S_3 near the origin. In all cases of practical interest, we expect S_3 to be a very smooth function of its arguments close to the origin and, therefore, the use of (44) to eliminate the singularities in (43) is fully justified.

Since all terms in (44) are nonsingular and the indicated integrations may be performed by a variety of methods, the main difficulty in evaluating (43) has been reduced to that of finding $a_2(r,s)$. Eq. (46) can be integrated directly using quadrature or other numerical procedures. However, several conditions special to this problem suggest that a least squares fitting technique would be preferable: (1) The function S_3 will nearly always be an empirical function so that a least squares method is natural. (2) The coefficients a_2 and a_4 are of comparable magnitude [13]; thus, a least squares method which calculates a_2 accurately must also calculate a_4 simultaneously. This fact is not detrimental, however, since both coefficients are needed anyway in applications to bounds on elastic constants. (3) A least squares method is very flexible as to the particular points used in evaluating the coefficients. This fact can be used to design an optimum routine which uses just the lattice points chosen earlier in this paper or convenient interpolated values.

Using the even and odd properties of the Legendre polynomials, we can eliminate the a_n 's for odd n by considering

$$a_0 + a_2 P_2(\mu_i) + a_4 P_4(\mu_i) + \dots = \frac{S_3(\mu_i) + S_3(-\mu_i)}{2} \equiv g(\mu_i) \quad (50)$$

where the radial arguments have been suppressed for simplicity. Using standard arguments [18], the least squares method results in the 3×3 matrix inversion problem

$$\begin{pmatrix} N & \sum_i P_2(\mu_i) & \sum_i P_4(\mu_i) \\ \sum_i P_2(\mu_i) & \sum_i P_2^2(\mu_i) & \sum_i P_2(\mu_i)P_4(\mu_i) \\ \sum_i P_4(\mu_i) & \sum_i P_2(\mu_i)P_4(\mu_i) & \sum_i P_4^2(\mu_i) \end{pmatrix} \begin{pmatrix} a_0 \\ a_2 \\ a_4 \end{pmatrix} = \begin{pmatrix} \sum_i g(\mu_i) \\ \sum_i g(\mu_i)P_2(\mu_i) \\ \sum_i g(\mu_i)P_4(\mu_i) \end{pmatrix} \quad (51)$$

where N is the total number of points $\mu_i \geq 0$ chosen and the total number of function evaluations is $2N$ (or $2N-1$ if $\mu = 0$ is one of the points). When a set of μ_i 's has been chosen, the matrix elements on the left hand side of (51) may be evaluated just once being independent of the values of r and s .

The choice of upper limit Δ_c is difficult in some cases since $a_2(r,s)$ does not vanish for large arguments if r and s are nearly equal. For example, note that it follows from the nature of S_3 [as in Eqs. (11) and (12)] that

$$S_3(\Delta, \Delta, \mu) \xrightarrow[\Delta \rightarrow \infty]{} S_2(t) \quad (52)$$

where $t = \Delta(2-2\mu)^{1/2}$. Substituting (52) into (46), it is easy to show that

$$a_2(\Delta, \Delta) = 0 \left(\frac{\phi^2(1-\phi)R^2}{\Delta^2} \right) \quad (53)$$

for $\Delta > R$ when R is a typical particle radius or correlation length. Thus, if we choose $\Delta_c = LR$ with $L = 2$ (for example), then the contributions to (46) from a wedge-shaped region with $(1-2R^2/r^2)^{1/2} \leq \mu \leq 1$ and $r = s > \Delta_c$ will be

neglected. The cumulative contribution from this wedge can be significant for large values of ϕ . To eliminate this difficulty, first note that for any function $h(t)$ with $t = (r^2 + s^2 - 2rs\mu)^{1/2}$ the following integral identity holds [14]

$$\int_0^\infty dr \int_0^\infty ds \int_{-1}^{+1} d\mu \frac{h(t)P_2(\mu)}{rs} = \frac{2}{9} [h(0) - h(\infty)]. \quad (54)$$

Since the troublesome terms have the form (52), we can add and subtract the quantity $\phi S_2(t)$ from $S_3(r,s,\mu)$. Then we find

$$\zeta_1 = \phi_1 + \frac{9I(a'_2)}{2\phi_0\phi_1} \quad (55)$$

where

$$a'_2(r,s) = \int_{-1}^{+1} d\mu [S_3(r,s,\mu) - \phi_1 S_2(t)] P_2(\mu). \quad (56)$$

With this definition, a'_2 vanishes much more rapidly than a_2 as $r \approx s \rightarrow \infty$ so a smaller value of Δ_C may be chosen when evaluating (55).

To test this algorithm and to provide an example of the ultimate usefulness of the three-point correlation functions, Eq. (55) has been evaluated for the penetrable sphere model (Sect. 3) using (44) and (51). The results are presented in Figure 13, where $\zeta = \zeta_1 = 1 - \zeta_0$ and σ^\pm are the upper and lower bounds on the conductivity when $\sigma_0 = 1.0$ and $\sigma_1 = 0.1$ corresponding to highly conducting spheres imbedded in a poorly conducting material. The integrals in (44) were performed using the adaptive Monte Carlo integration

procedure VEGAS [19] used previously for computing variational bounds on permeability for aggregates of spheres [20]. For the penetrable sphere model, $\Delta_c \geq 2R$ and typically $\Delta_c = 3R$ or $4R$. The lower limit Δ_0 was chosen to be in the range $0.02 \leq \Delta_0/R \leq 0.08$. The parameters for VEGAS were the same as in [20] except that the target accuracy for each integration was set at 1%.

Various tests of our numerical method have been considered. One very convenient check on the integration routine again makes use of the identity (54). By substituting $S_2^2(t)/\phi_1$ for $S_3(r,s,\mu)$ in (56), we find easily that in this case

$$I(a'_2) = \frac{2}{9} \phi_1 (1 - \phi_1^2) \quad (57)$$

since $S_2^2(0)/\phi_1 = \phi_1$ and $S_2^2(\infty)/\phi_1 = \phi_1^3$. The function $S_2^2(t)/\phi_1$ is not at all a good estimate of S_3 but it does have the same values at the origin and at infinity. This test case was used to provide some insight into the optimum choice of parameters at each value of ϕ_1 studied. Another check on the results is the published table of values for the same integral provided by Torquato and Stell [8]. Our calculated values agree well with those in [8]. Furthermore, we expect $\zeta \rightarrow \phi_1$ as $\phi_1 \rightarrow 1$ since in this limit the particles become well-separated spheres and Milton [13] has pointed out that $\zeta_0 = \phi_0$ in this case. Figure 13 shows that $\zeta_1 \rightarrow \phi_1$ as expected for $\phi_1 > 0.95$.

One important lesson learned from the penetrable sphere example is that the bounds are not very sensitive functions of ζ . In most cases, a 5% change in ζ (at fixed ϕ) leads to less than a 1% change in either σ^\pm . The fact that the functions (39) and (40) tend to narrow the error bars in the final result

is encouraging because the empirically derived three-point correlation functions may not be known very accurately so we may not expect to have highly accurate values of ζ in general.

7. DISCUSSION

General methods for processing images of surfaces of random two-phase composite materials have been developed in this paper. The only examples used in the text were those for the penetrable sphere model; however, the methods developed are in no way restricted to this case. The penetrable sphere model is just a very convenient test case - unique because the analytical solutions are known for the spatial correlation functions and because model images of cross sections of the material are easily generated by computer.

The methods presented here may be generalized for multiphase composites but the corresponding discussion for preprocessing of the digitized image (Sect. 4) will be considerably more complex due to difficulties with resolution. Furthermore, the major remaining obstacle to application of these techniques to real two-phase materials is again one of resolution if the constituents' colors are not "black" and "white" as assumed here. However, the resolution problem is not so much an image processing problem as a sample surface preparation problem which should be solved in the laboratory prior to photographing the surface. Such work is in progress and will be reported elsewhere.

Acknowledgments

I wish to thank the Signal and Image Processing Research Group - especially C. H. Journeay, R. K. Oberman, M.R. Portnoff, R.J. Sherwood, and R.E. Twogood - for their hospitality and help at various critical junctures in the development of this technique. Work performed under the auspices of the U.S. Department of Energy by the Lawrence Livermore National Laboratory under Contract W-7405-ENG-48 and supported specifically by the Base Technology Program of the Earth Sciences Department.

References

1. W. F. Brown, Jr., J. Chem. Phys. 23 (1955), 1514.
2. S. Prager, Phys. Fluids 4 (1961), 1477.
3. M. J. Beran, "Statistical Continuum Theories," Interscience, New York, 1968.
4. P. B. Corson, J. Appl. Phys. 45 (1974), 3159.
5. S. Torquato and G. Stell, J. Chem. Phys. 77 (1982), 2071.
6. H.L. Weissberg, J. Appl. Phys. 34 (1963), 2636.
7. M. Uoi, J. Phys. Soc. Japan 40 (1976), 567.
8. S. Torquato and G. Stell, J. Chem. Phys. 79 (1983), 1505.
9. H.L. Weissberg and S. Prager, Phys. Fluids 5 (1962), 1390.
10. M.J.D. Powell, Mol. Phys. 7 (1964), 591.
11. R.K. Guy, "Unsolved Problems of Number Theory," Springer-Verlag, New York, 1981, p. 131.
12. J. Hammer, "Unsolved Problems Concerning Lattice Points," Pittman, London, 1977.
13. G.W. Milton, Phys. Rev. Lett. 46 (1981), 542.
14. G.W. Milton, J. Mech. Phys. Solids 30 (1982), 177.
15. J.G. Berryman, "Bounds on fluid permeability for viscous flow through porous media," LLNL UCRL-90929, June, 1984.
16. J.G. Berryman, "Variational bounds on elastic constants for the penetrable sphere model," LLNL UCRL-91115, June, 1984.
17. J.G. Berryman, in "Elastic Wave Scattering and Propagation," edited by V.K. Varadan and V.V. Varadan, Ann Arbor Science, Ann Arbor, MI, 1982, Chapt. 7.
18. F.B. Hildebrand, "Introduction to Numerical Analysis," McGraw-Hill, New York, 1956, Chapt. 7.
19. G.P. Lepage, J. Comput. Phys. 27 (1978), 192.
20. J.G. Berryman, J. Comput. Phys. 52 (1983), 142.

ℓ	No. of Triangles	Storage Requirement (T_ℓ)	ℓ	No. of Triangles	Storage Requirement (T_ℓ)
0	1	1	17	92	621
1	1	2	18	111	732
2	3	5	19	115	847
3	4	9	20	138	985
4	8	17	21	139	1124
5	10	27	22	164	1288
6	16	43	23	167	1455
7	16	59	24	191	1646
8	25	84	25	199	1845
9	27	111	26	225	2070
10	39	150	27	231	2301
11	40	190	28	259	2560
12	51	241	29	264	2824
13	55	296	30	297	3121
14	70	366	31	300	3421
15	74	440	32	336	3757
16	89	529	33	341	4098

Table 1. Number of triangles in the minimal set of lattice-commensurate triangles with longest side equal to ℓ units. The cumulative total for all cases with longest side less than or equal to ℓ determines the required storage capacity T_ℓ .

2	0	0	0	0	0	0	0	0	0	0	0	0	0	0	0	0
3	0	0	0	0	0	0	0	0	0	0	0	0	0	0	0	0
3	4	0	0	0	0	0	0	0	0	0	0	0	0	0	0	0
4	5	0	0	0	0	0	0	0	0	0	0	0	0	0	0	0
4	5	6	0	0	0	0	0	0	0	0	0	0	0	0	0	0
4	5	6	0	0	0	0	0	0	0	0	0	0	0	0	0	0
4	6	7	7	0	0	0	0	0	0	0	0	0	0	0	0	0
5	6	7	8	0	0	0	0	0	0	0	0	0	0	0	0	0
5	7	8	9	9	0	0	0	0	0	0	0	0	0	0	0	0
5	7	8	9	10	0	0	0	0	0	0	0	0	0	0	0	0
5	7	8	9	10	11	0	0	0	0	0	0	0	0	0	0	0
6	7	9	10	11	11	0	0	0	0	0	0	0	0	0	0	0
6	8	9	10	11	12	13	13	0	0	0	0	0	0	0	0	0
6	8	10	11	12	13	13	13	0	0	0	0	0	0	0	0	0
6	8	10	11	12	13	14	14	14	0	0	0	0	0	0	0	0
6	9	10	11	13	13	13	14	15	0	0	0	0	0	0	0	0
6	9	10	12	13	14	15	15	15	16	0	0	0	0	0	0	0
7	9	11	12	13	14	15	15	16	17	0	0	0	0	0	0	0
7	9	11	13	14	15	16	17	17	18	0	0	0	0	0	0	0
7	9	11	13	14	15	16	17	18	18	0	0	0	0	0	0	0
7	10	12	13	14	16	17	17	18	19	19	20	0	0	0	0	0
7	10	12	13	15	16	17	18	19	19	19	20	0	0	0	0	0
7	10	12	14	15	16	17	18	19	19	20	21	21	0	0	0	0
8	10	12	14	16	17	18	19	20	21	21	21	22	0	0	0	0
8	11	13	14	16	17	18	19	20	21	21	22	22	23	0	0	0
8	11	13	15	16	17	19	20	21	21	22	22	23	24	0	0	0
8	11	13	15	16	18	19	20	21	21	22	23	23	24	25	0	0
8	11	13	15	17	18	19	21	22	22	23	23	24	24	25	25	0
8	11	14	15	17	19	20	21	22	23	23	24	24	25	25	26	0
8	11	14	16	17	19	20	21	22	23	23	24	24	25	26	26	0
8	12	14	16	18	19	20	22	23	24	24	25	25	26	26	27	0
8	12	14	16	18	19	21	22	23	24	24	25	26	27	27	28	0

Table 2. The matrix M_{zp} for $2 \leq z \leq 32$ and $1 \leq p$.

Note that $M_{z0} = 1$ for all z . See Eq. (36).

FIGURE CAPTIONS

Figure 1. Computer simulation of a cross section of a penetrable sphere material with volume fraction $\phi = 0.35$ and $\rho = 8000$ (in dimensionless units) including the frame.

Figure 2. Digitized images of a simulated cross section of penetrable sphere material with volume fraction $\phi = 0.31$. (a) Digitized negative image after the frame has been removed. (b) Digitized positive image containing only zeroes and ones.

Figure 3. Details of Figure 2. (a) Illustration of the color spread at particle interfaces. (b) Illustration of the discrete nature of the interface after a threshold is chosen.

Figure 4. Histogram of pixel values for Figure 2(a).

Figure 5. Digitized images of a simulated cross section of penetrable sphere material with volume fraction $\phi \approx 0.18$. (a) Digitized positive image before choosing threshold. (b) Digitized positive image after choosing threshold.

Figure 6. Details of the model in Figure 5. (a) Example of choosing threshold too low, creating porosity in center of particles. (b) Example of a better choice of threshold.

Figure 7. Illustrating the algorithm for obtaining the isotropic two-point correlation function from the computed values at lattice points for a particular image. See Eqs. (25) and (26).

Figure 8. Measured two-point correlation function S_2 for the photograph in Figure 2. The averaged S_2 obtained using (26) is the solid line. The expected value for S_2 calculated using (14) and (16) for $\phi = 0.31$ is the dashed line. For comparison, the two extreme estimates $\hat{S}_2(0,k)$ and $\hat{S}_2(k,0)$ are shown as the dot-dash and long-dash/short-dash lines.

Figure 9. All triangles with longest side $L = 6$ may be arranged on the diagram so that the vertex opposite the longest side lies inside the shaded area. Values of S_3 for other triangles such as the right triangle shown (with sides 3, 5, and 5.83 units) may be obtained by interpolation from the triangles in the minimal subset of lattice-commensurate triangles.

Figure 10. Sequence of diagrams used to determine the minimal set of lattice-commensurate triangles for L up to $L = 9$.

Figure 11. Three possible stencils which may be used to calculate the three-point correlation function for the triangle $(L, M, N) = (3, 1, 1)$.

Figure 12. Measured three-point correlation functions for the synthetic material in Figure 2, using only 204 lines of the image in (a) and 510 lines in (b).

Figure 13. The zeta Milton number ζ and the upper (σ^+) and lower (σ^-) bounds on conductivity when $\sigma_0 = 1.0$ and $\sigma_1 = 0.1$ as a function of volume fraction ϕ .

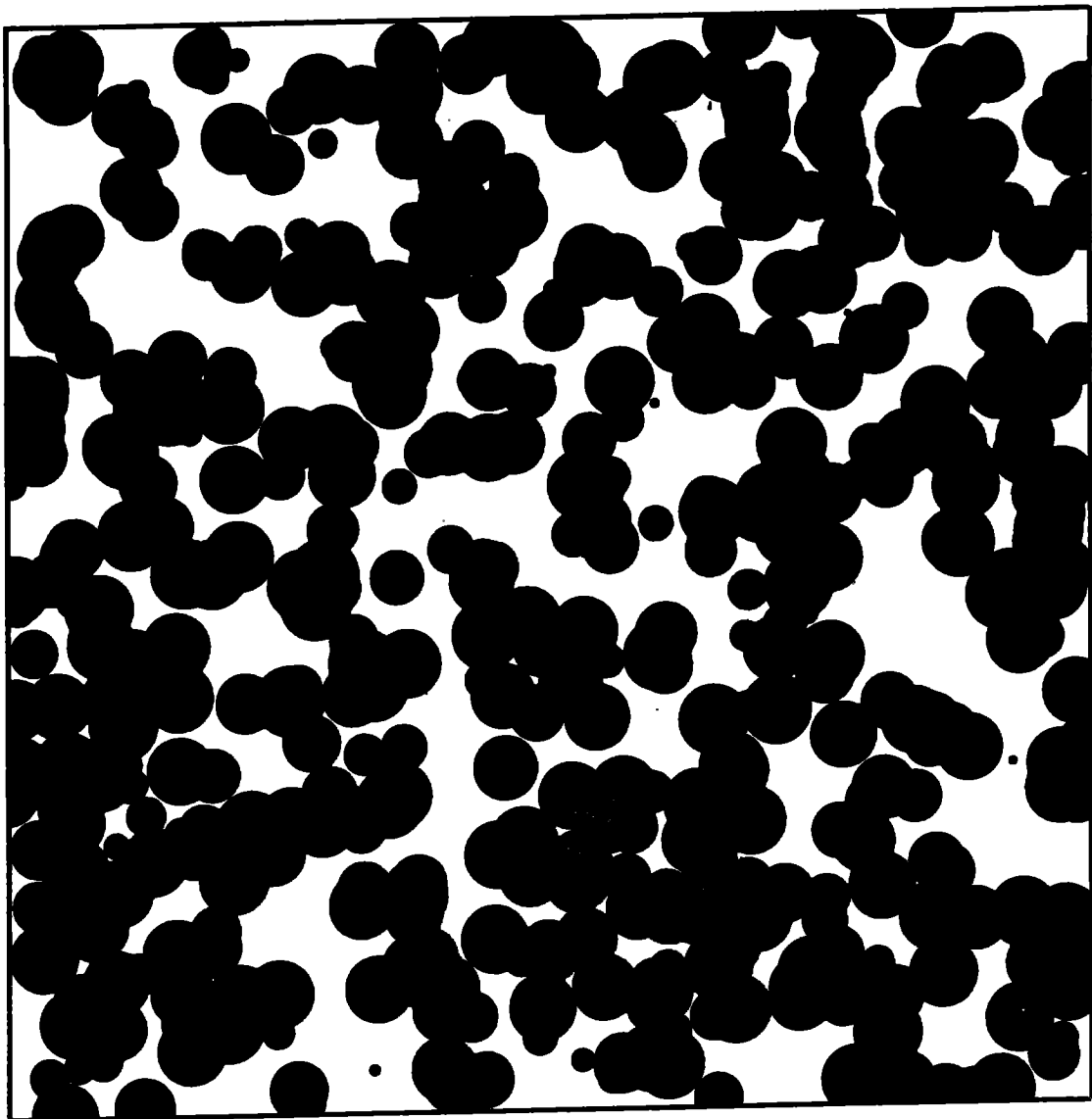
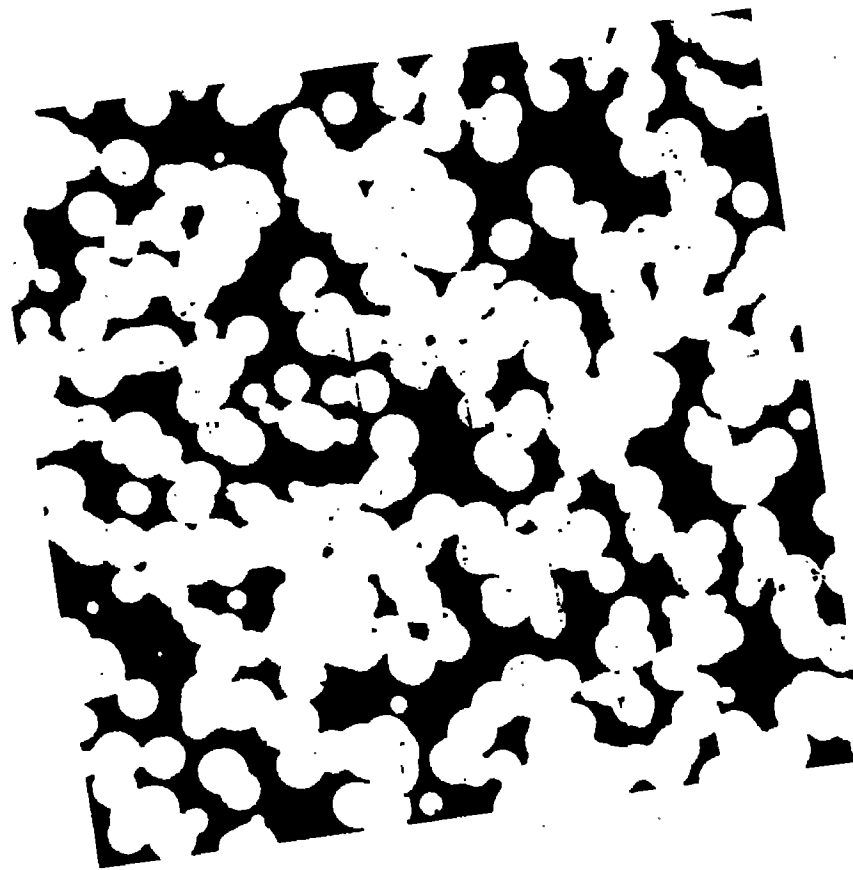
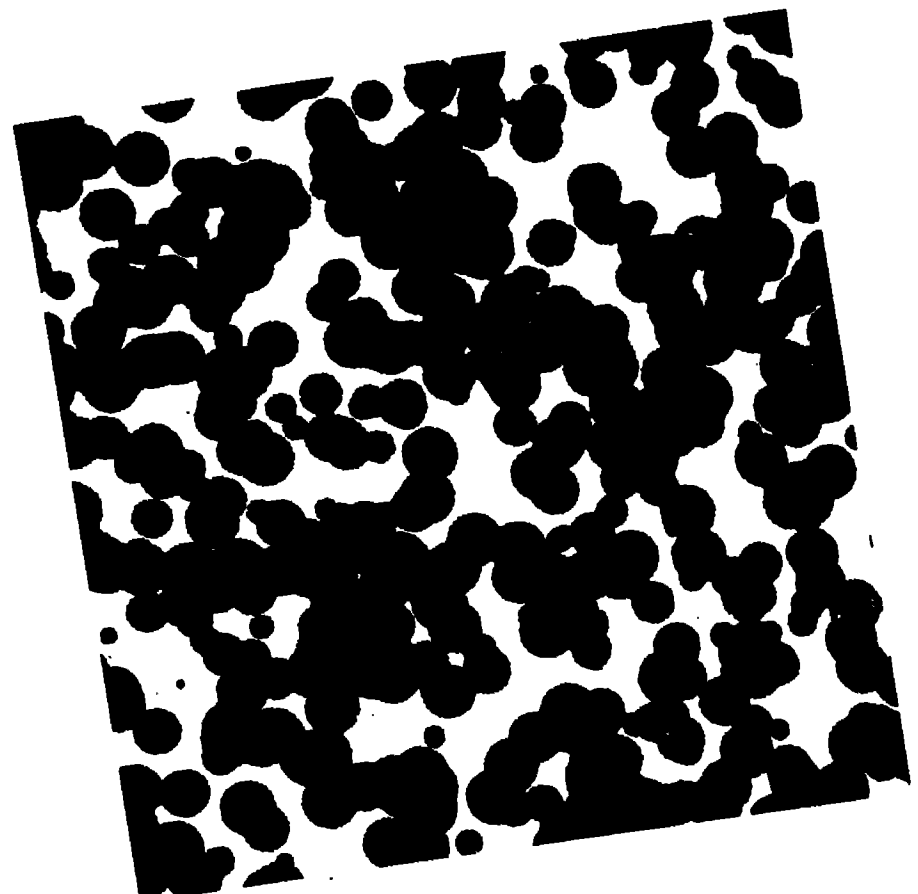


FIGURE 1

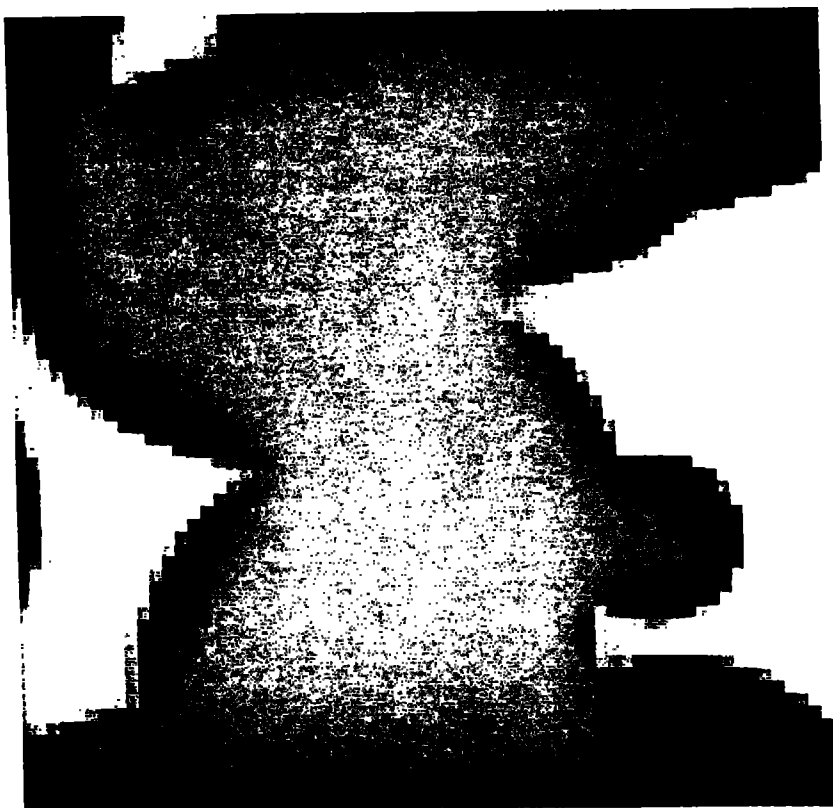


(a)

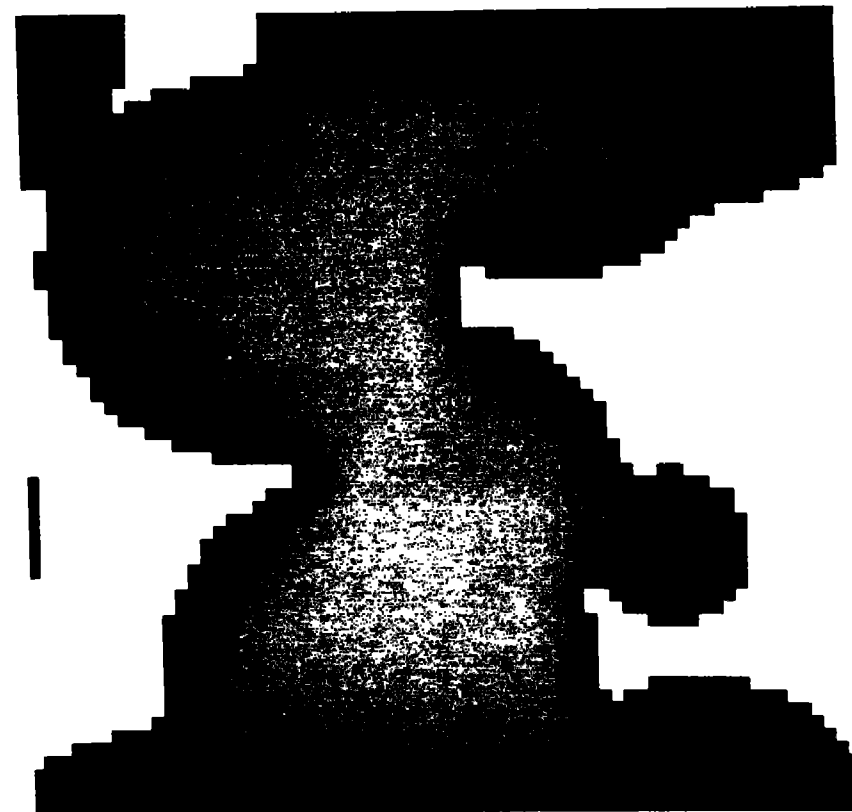


(b)

FIGURE 2.



(a)



(b)

FIGURE 3.

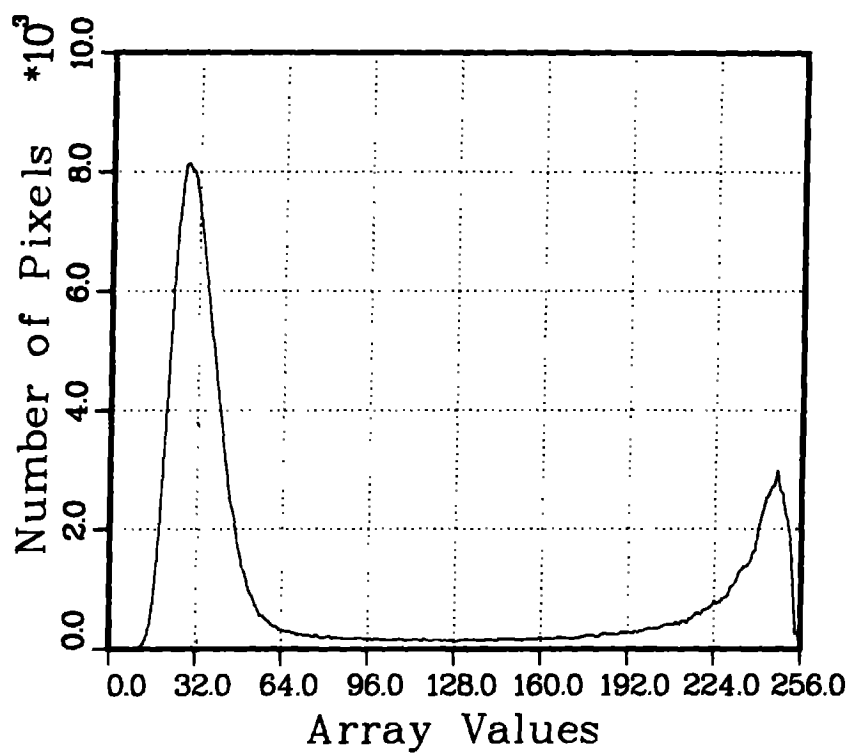
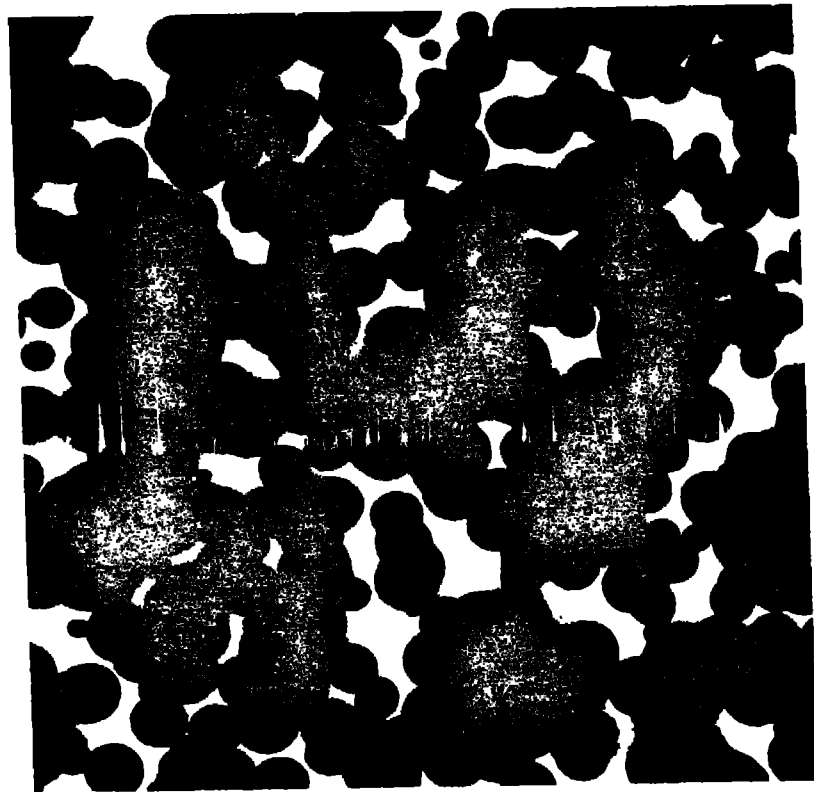
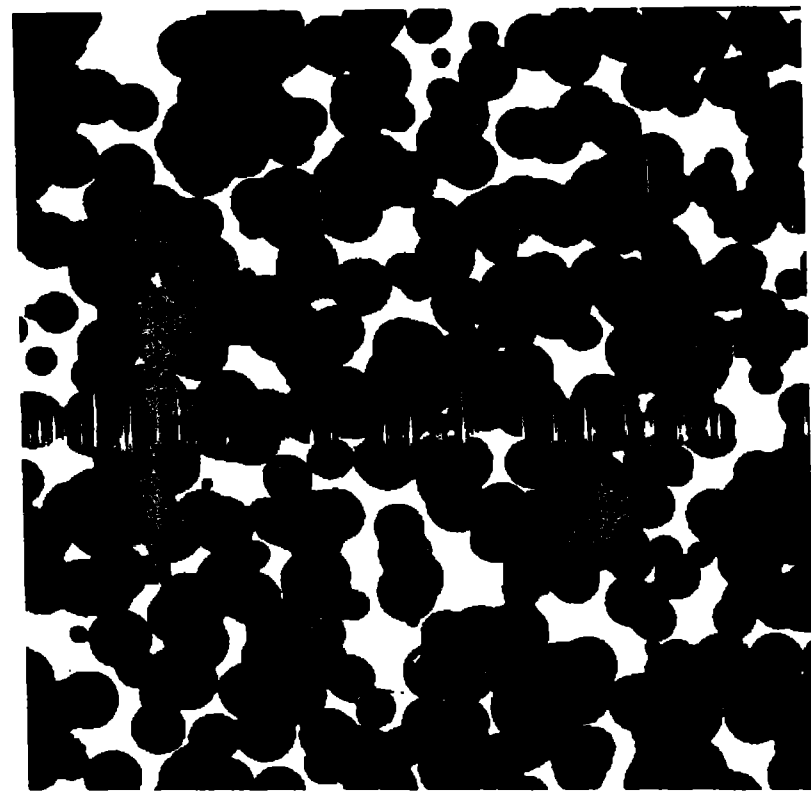


FIGURE 4



(a)

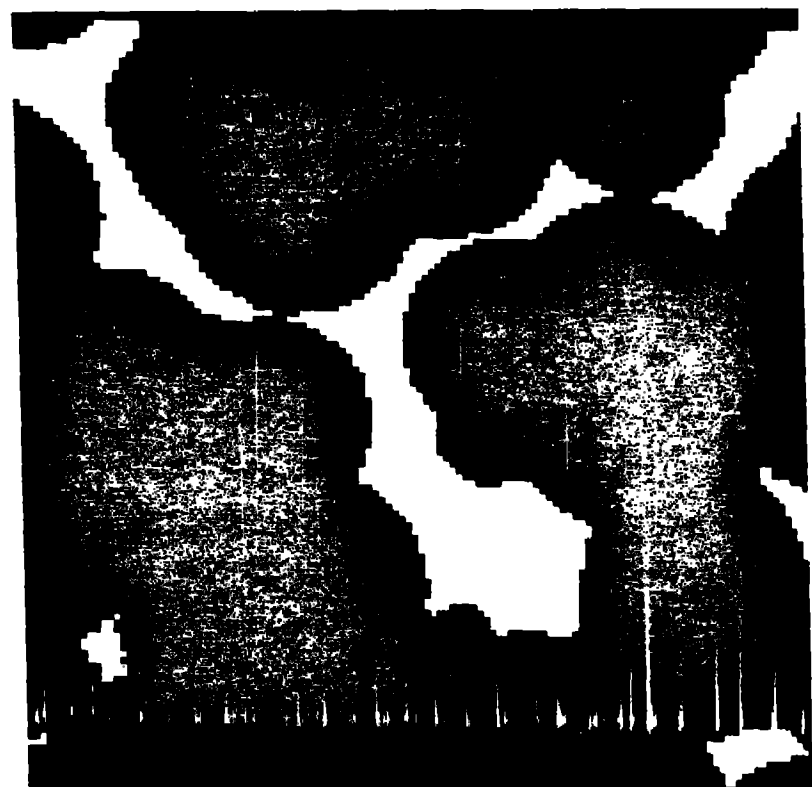


(b)

FIGURE 5.



(a)



(b)

FIGURE 6.

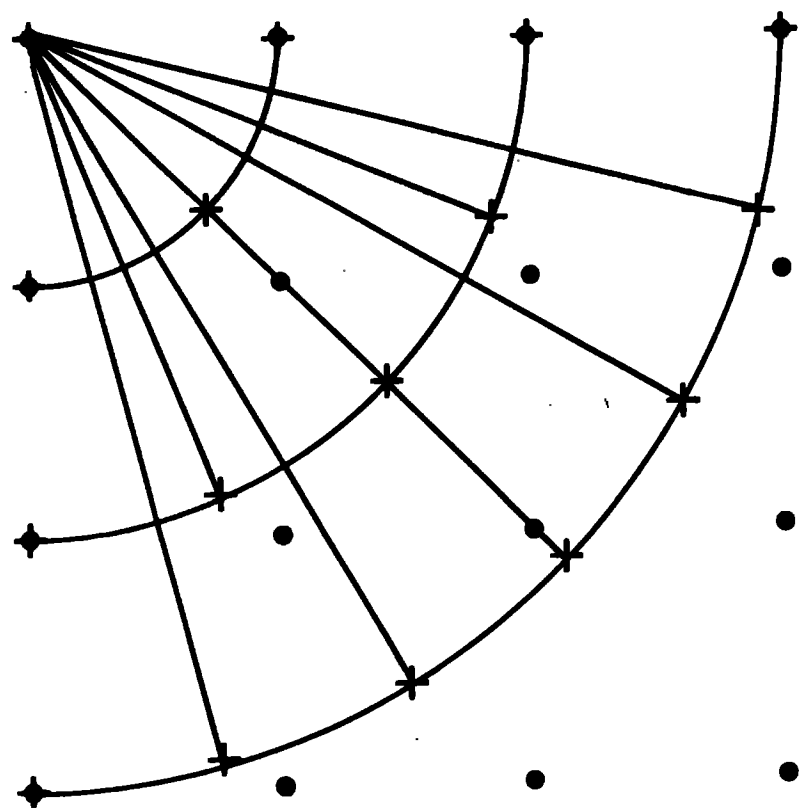


FIGURE 7

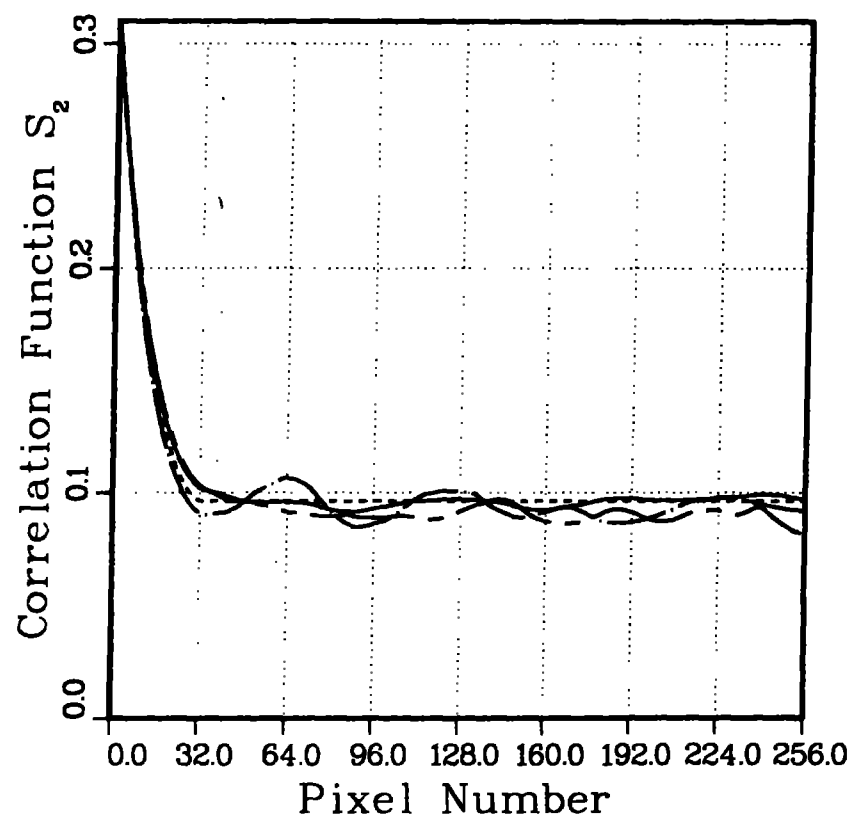


FIGURE 8

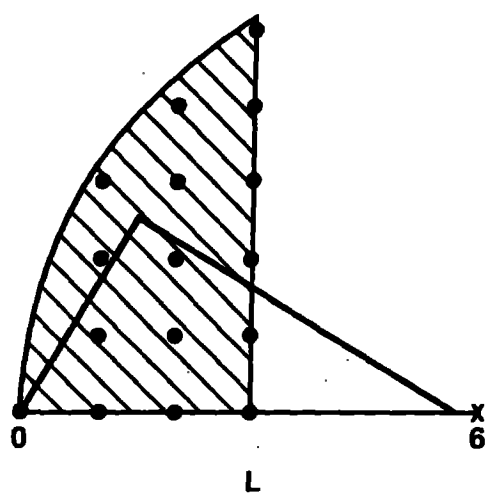


FIGURE 9

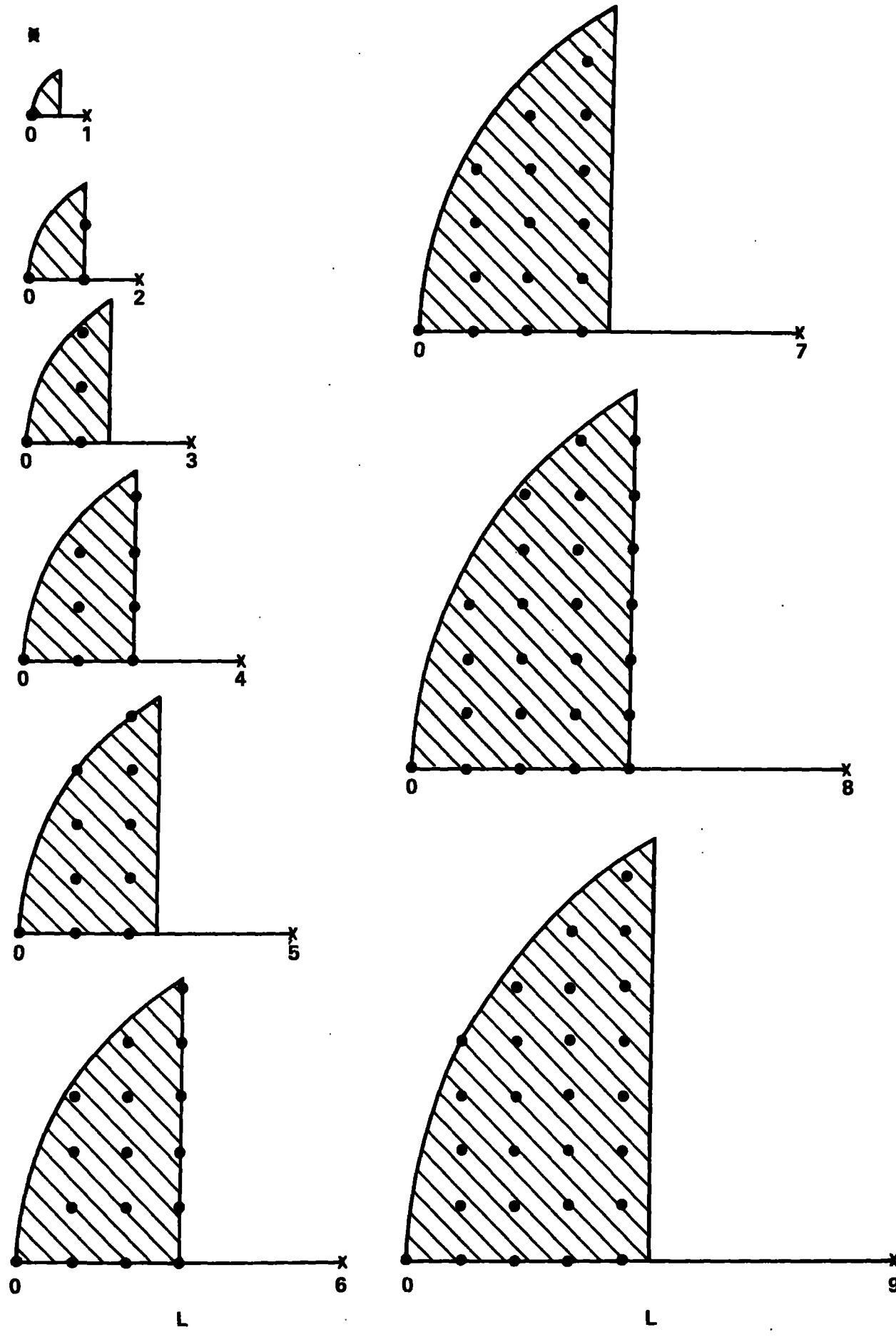


FIGURE 10

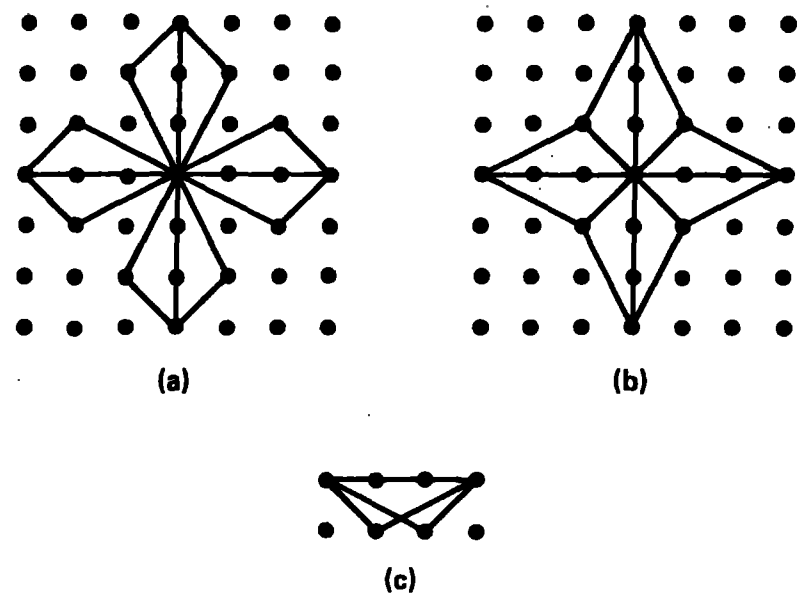


FIGURE 11

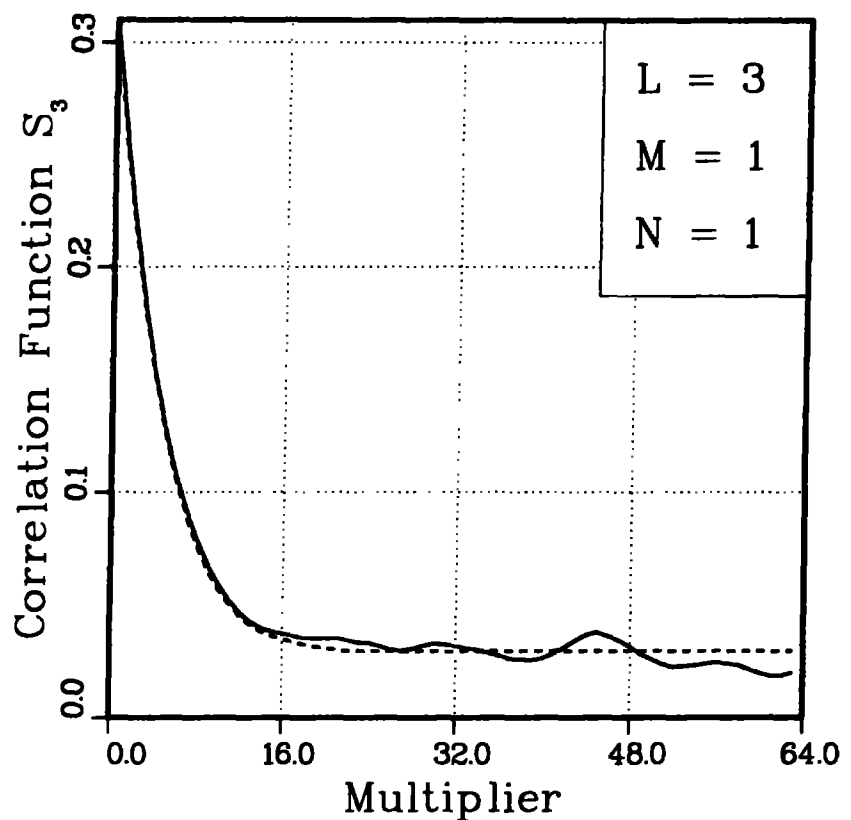


FIGURE 12(a)

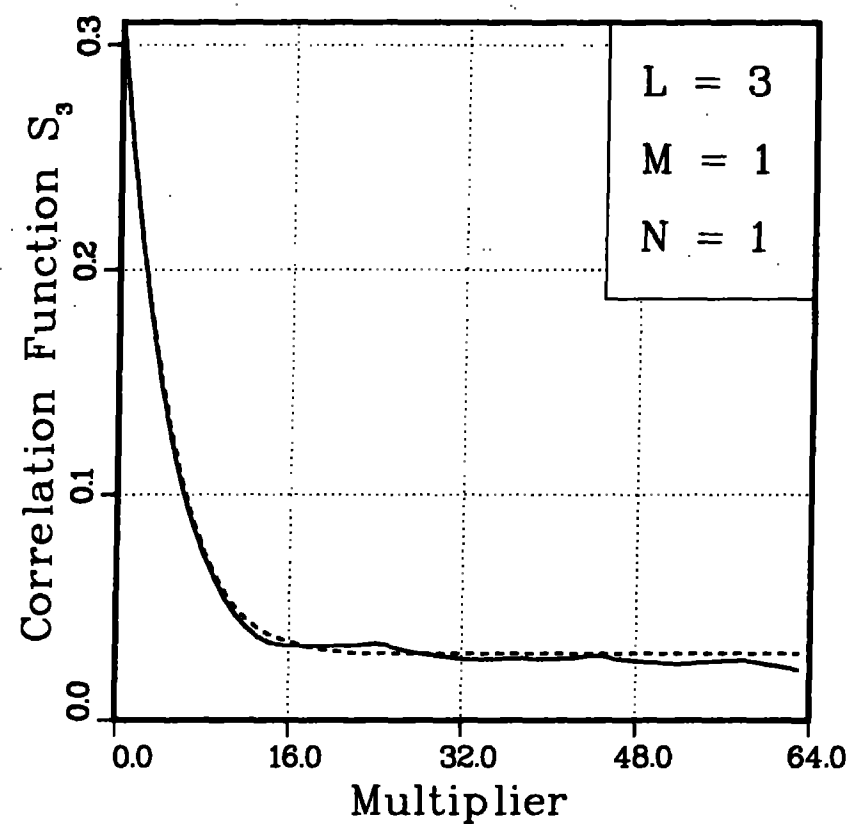


FIGURE 12(b)

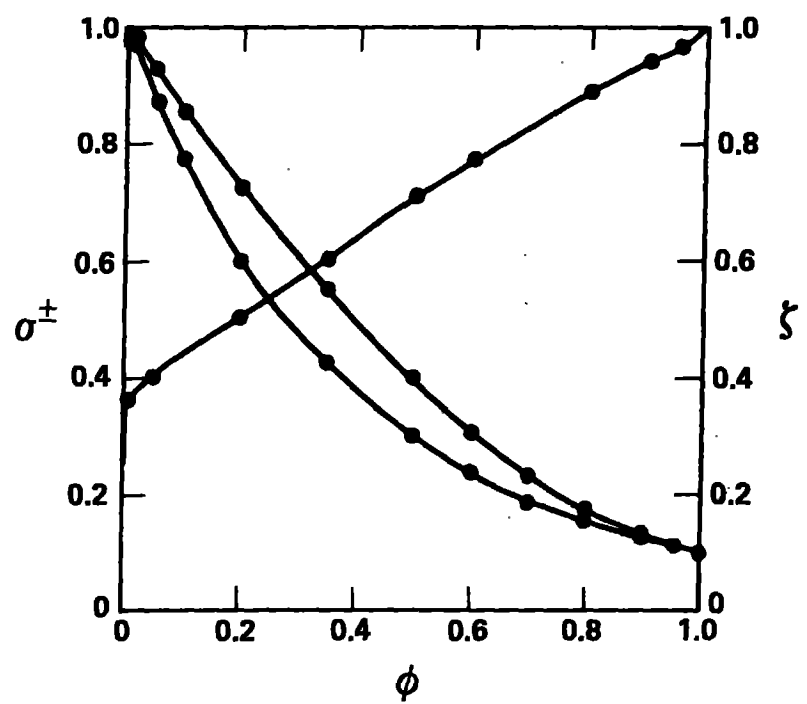


FIGURE 13